Applied Energy 288 (2021) 116641

Contents lists available at ScienceDirect

Applied Energy

journal homepage: www.elsevier.com/locate/apenergy

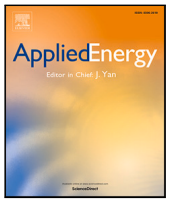

Spatiotemporal wind field prediction based on physics-informed deep learning and LIDAR measurements

Jincheng Zhang, Xiaowei Zhao *

Intelligent Control & Smart Energy (ICSE) Research Group, School of Engineering, University of Warwick, Coventry, UK

ARTICLE INFO

Keywords:
Deep learning
LIDAR measurements
Physics-informed neural networks
Wind field prediction

ABSTRACT

Spatiotemporal wind field information is of great interest in wind industry e.g. for wind resource assessment and wind turbine/farm monitoring & control. However, its measurement is not feasible because only sparse point measurements are available with the current sensor technology such as LIDAR. This work fills the gap by developing a method that can achieve spatiotemporal wind field predictions by combining LIDAR measurements and flow physics. Specifically, a deep neural network is constructed and the Navier–Stokes equations, which provide a good description of atmospheric flows, are incorporated in the deep neural network by employing the physics-informed deep learning technique. The training of this physics-incorporated deep learning model only requires the sparse LIDAR measurement data while the spatiotemporal wind field in the whole domain (which cannot be measured) can be predicted after training. This study, which can discover complex wind patterns that do not present in the training dataset, is totally distinct from previous machine learning based wind prediction studies which treat machine learning models as “black-box" and require the corresponding input and target values to learn complex relations. The numerical results on the prediction of the wind field in front of a wind turbine show that the proposed method predicts the spatiotemporal flow velocity (including both downwind and crosswind components) in the whole domain very well for a wide range of scenarios (including various measurement noises, resolutions, LIDAR look directions, and turbulence levels), which is promising given that only line-of-sight wind speed measurements at sparse locations are used.

1. Introduction

As one of the most important renewable energy resources, wind energy is under fast development all over the world. While driving large mechanical devices (such as horizontal-axis wind turbines) to generate power, wind is also the main source of disturbance that causes damages to these devices and undermines the quality of the generated electricity. In order to make good use of the incoming wind and to mitigate the impact of the disturbance, wind speed measurement technologies, such as light detection and ranging (LIDAR) [1], have been developed in recent years. Extensive research efforts have since then been spent in the measurement analysis of LIDAR [2,3] and their applications in wind turbine control [4,5] and wind resource assessment [6,7]. However, LIDAR can only provide wind speed measurements at sparse spatial locations along the laser beam. As pointed out in [8], it can only measure the line-of-sight (LoS) wind speed in the laser beam direction, so the wind speed magnitude and direction have to be estimated (Cyclops’ dilemma). Thus the spatiotemporal wind field measurement is out of reach with the current sensor technologies. On the other hand, the detailed wind information is of great interest because it can offer brand new opportunities in wind industry e.g. developing strategies on the wind resource assessment and the monitoring and control of wind turbine/farm. For example, detailed wind information was investigated based on CFD simulations for the wind resource assessment of complex terrains in [9,10] while the control of wind turbines based on detailed flow structures was studied in [11] which showed the detailed wind information could improve the control performance significantly. Therefore, this work aims to bridge the gap between the limitation of the current wind measurement technology and the need of spatiotemporal wind information in various applications, by developing a deep learning based method that can predict the spatiotemporal wind field in the whole flow domain through combining LIDAR measurement and flow physics.

Currently there are very limited studies on unsteady wind field predictions from LIDAR measurements. In [12], a wind field reconstruction method was proposed, where a simplified dynamic model of the atmospheric boundary layer was derived and then an unscented Kalman filter (UKF) was used to estimate the model state from LIDAR measurements. The sensitivity study of the developed method was also carried

* Corresponding author.
E-mail addresses: jincheng.zhang@warwick.ac.uk (J. Zhang), xiaowei.zhao@warwick.ac.uk (X. Zhao).

https://doi.org/10.1016/j.apenergy.2021.116641
Received 15 October 2020; Received in revised form 28 December 2020; Accepted 7 February 2021
Available online 17 February 2021

out, where different beam half-angles, look directions, atmosphere conditions, and measurement noise levels were considered. In [13], a velocity and pressure field estimation framework was proposed, where a reduced order dynamic model was built based on Navier–Stokes (NS) equations, by uniquely employing a pressure Poisson equation formulation in conjunction with a basis function decomposition method. Then a modified UKF algorithm was used for the state estimation. The proposed method was validated by both numerical experiments and real-world LIDAR measurements.

The aforementioned studies employed traditional approaches and relied on either low-fidelity flow models or reduced order modeling of NS equations. Thus the prediction accuracy was undermined. In this work, machine learning approach will be employed with NS equations being directly encoded into the wind field prediction process, which can approximate the complex nonlinear dynamics of the incoming wind without model reduction.

Machine learning, in particular deep learning [14], is developing very fast in the past few years, and its applications in wind industry have also seen great successes e.g. in wind power forecasting [15], wind speed forecasting [16,17], and wind farm wake modeling [18,19]. However, the incorporation of physical laws in the training of deep learning models has not been explored in wind energy studies while such ideas are emerging in other physical systems such as the data-based turbulence modeling [20,21], the discovery of governing equations [22,23], solving high-dimension partial differential equations (PDEs) [24] and the surrogate modeling of physical systems [25,26]. Recently a versatile machine learning framework for solving forward and inverse problems involving PDEs, called physics-informed neural networks (PINNs), was proposed in [27]. The main idea of PINNs is to encode PDEs in terms of loss functions, which are then used for neural network (NN) training together with the available labeled data. Specifically, automatic differentiation [28] is employed to take the derivatives of the NN output with respect to the NN input (i.e. space and time coordinates). These derivatives are then used to form the loss functions that represent the residues of the PDEs. The development of PINNs is becoming very active. Recent studies include both method development (such as its uncertainty quantification [29], the use of adaptive activation functions [30] and the learning from multi-fidelity [31] and noisy data [32]) and various applications (such as vortex-induced vibrations [33], high-speed flow [34], and hidden-physics inference from flow visualizations [35]).

In this work, following the PINNs framework [27], a deep learning based method is proposed for the predictions of spatiotemporal wind field using only LIDAR measurements at sparse locations. Here the NS equations are encoded in the deep NN and an observation process is embedded into the NN which maps the full flow state to LIDAR observations. The NN training is carried out to minimize both the functional loss (which encodes the NS equations) and the measurement loss (which is based on LIDAR observations). We distinguish our method with traditional numerical methods and existing machine learning based wind prediction methods as follows: (1) Various numerical models e.g. [36–38] are widely used for wind simulations and the detailed wind field can be obtained by solving the NS equations numerically with properly-defined boundary conditions or the input conditions estimated from measurement data [39]. However, these models are mainly designed for forward simulations of wind flows. It is extremely challenging to incorporate real-time scattered measurement data in these models because it involves solving the inverse problem, which would require a formidable number of time-consuming simulations to calibrate the model parameters and the input conditions against the measurement data. In contrast, the PINNs framework is specifically designed to incorporate data and PDEs in a unified manner which makes it very powerful in solving inverse problems governed by PDEs. (2) Previous machine learning based wind prediction studies e.g. [16,18,40] treat machine learning models as "black-box" and require the corresponding input and target values for training. Then they can predict the wind patterns which are present in the training dataset. We mention that the paper [40] did explore to involve physics in the form of simple analytical relations in the design of the machine learning on the wind farm modeling, which showed very promising results. However, all these studies followed the traditional supervised machine learning, thus cannot discover the wind patterns that are not present in the measurement data. In summary, our work, which fuses physics in terms of PDEs and data in the deep learning training process for wind applications for the first time, can achieve the predictions of spatiotemporal wind field in the whole domain based on only line-of-sight LIDAR measurements at sparse spatial locations, which is not achievable by either traditional numerical models or existing machine learning based models in the literature.

The method proposed in this work is tested and validated using large-scale numerical simulations based on SOWFA (Simulator for Onshore/Offshore Wind Farm Applications) [41]. SOWFA is a numerical solver based on OpenFOAM for the 3D large eddy simulation (LES) of wind flow around wind turbine array in the atmospheric boundary layer, which is developed by National Renewable Energy Laboratory. It is widely used [41] and has been validated in various studies such as the study of the turbine dynamics [42] and the control of wind farms [43]. It is used in this work as the high-fidelity numerical experiment platform to simulate the real-world wind flows in the atmospheric boundary layer. The LIDAR measurement and the turbulent wind field are extracted from SOWFA simulations as the model training data and the ground truth (for model validation) respectively. The results show that the proposed method can predict the spatiotemporal wind field very well, including both the wind magnitude and direction predictions. In particular, the propagation of the high-speed/low-speed flow structures in the incoming wind is accurately predicted, which is of great importance for wind turbine control. To further demonstrate the method's robustness, a sensitivity analysis is also carried out, where LIDAR measurements with various levels of noise and under different LIDAR spatial/temporal resolutions, different LIDAR look directions and different freestream turbulence intensity (FSTI) levels are considered. The results show that the proposed method performs very well under all the scenarios considered.

The main contributions and novelties of this paper are summarized as follows:

(1) **The prediction of spatiotemporal wind velocity field in the whole flow domain based on line-of-sight wind speed at only a few sparse locations measured by LIDAR is achieved, which is of great importance for developing advanced approaches for the wind resource assessment and for the monitoring and control of wind turbine/farm.** The developed method can achieve: (i) the prediction of flow dynamics over the whole domain of interest, including the spatial locations where no measurements are available; (ii) great accuracy in wind field estimation, because the spatiotemporal correlations between measurements are taken into account implicitly through NS equations without model reduction; (iii) robust wind estimation in the scenarios of both "small" and "big" data, as the issue of overfitting commonly encountered in deep learning is tackled by enforcing the physical constraints.

(2) **To our knowledge, this is for the first time that physical laws (in terms of PDEs) and data are fused in the training of deep learning models for wind applications.** Specifically a deep NN with a large degree of freedom is constructed and then the NS equations (which provide a good description of atmospheric flows) are incorporated directly in the deep NN. After that, the deep NN is trained to minimize the errors from both fitting the LIDAR measurements and enforcing the NS equations. Because the existing wind prediction studies are either purely data-driven [16,17] or based on low-fidelity/reduced order models [12,13], they cannot take full advantage of both physical laws in terms of PDEs and data.

Table 1
The main terminologies (including abbreviations, parameters and variables) mentioned in this paper.

List of terminologies (abbreviations)			
DoF	Degree of freedom	NN	Neural network
FSTI	Freestream turbulence intensity	NS	Navier–Stokes
HPC	High-performance computing	PDE	Partial differential equation
LES	Large eddy simulation	PINN	Physics-informed neural network
LIDAR	Light detection and ranging	SOWFA	Simulator for Offshore Wind Farm Applications
LoS	Line-of-sight	UKF	Unscented Kalman filter
MRMSE	Mean value of the root-mean-squared errors		
List of terminologies (parameters and variables)			
B_i	The bias term in the NN	$\hat{u}$	The prediction value of the wind magnitude
D	The turbine rotor diameter	u^*	The true value of the wind magnitude
$\tilde{\mathscr{D}}$	The dataset of all the NS test points	U_∞	The average freestream wind speed
$\mathscr{D}$	The nondimensionalized $\tilde{\mathscr{D}}$	$\bar{U}$	The effective wind speed
$L+1$	The total number of layers in the NN	$\tilde{\mathscr{U}}^l$	All the LIDAR measurements by the left beam
$\mathscr{L}_1$	The loss arising from NS residue terms	$\mathscr{U}^l$	Nondimensionalized left beam data
$\mathscr{L}_2$	The loss arising from LIDAR observations	$\tilde{\mathscr{U}}^r$	All the LIDAR measurements by the right beam
$\mathscr{L}$	The total NN loss	$\mathscr{U}^r$	Nondimensionalized right beam data
N_{dof}	The total DoF of the NN	W_i	The weight matrix in the NN
N_{d_1}	The batch size for right-beam test points	$[\tilde{x}^l, \tilde{y}^l]$	The spatial coordinate of points in the left beam
N_{d_2}	The batch size for left-beam test points	$[\tilde{x}^r, \tilde{y}^r]$	The spatial coordinate of points in the right beam
N_{ns}	The batch size for NS residue terms	$[x^{ns}, y^{ns}, t^{ns}]$	The test points to evaluate NS residue terms
N_h	The neuron number of the hidden layers	ϵ_u	The MRMSE of the predicted wind magnitude
N^l	The total number of points in the left beam	ϵ_γ	The MRMSE of the predicted wind direction
N^r	The total number of points in the right beam	$\hat{\gamma}$	The prediction value of the wind direction
N_{test}	The total number of NS test points	γ^*	The true value of the wind direction
T	The total time period	ν	The kinematic viscosity of air
$\tilde{u}$	The LIDAR measurement values	ψ	The stream function
u^r_{los}	NN output of the LoS speed in the right beam	σ	The activation function in the NN
u^l_{los}	NN output of the LoS speed in the left beam		

(3) **The developed method is validated through high-fidelity LES wind farm simulations and its robustness is verified under a wide range of scenarios.** The results show that the proposed method predicts the spatiotemporal flow velocity in the whole flow domain very well for all the considered scenarios including LIDAR measurements with various levels of noise and under different LIDAR spatial/temporal resolutions, different LIDAR look directions and different FSTI levels. Both the wind magnitude and direction are accurately predicted by using only the LoS LIDAR measurements, overcoming the Cyclops' dilemma. A short-term wind forecasting is also achieved which does not rely on the Taylor's frozen turbulence hypothesis [44], as the NN learns the dynamics of the evolving wind field from NS equations.

The remaining part of this paper is organized as follows: the deep learning based method for the spatiotemporal wind field predictions is described in Section 2. Then the performance of the proposed method is tested by using an LES wind farm simulator as the experimental platform in Section 3, where a wide range of scenarios are considered to verify the robustness of the proposed method. Finally the conclusions are drawn in Section 4. The main terminologies mentioned in this paper are presented in Table 1.

2. Methodology

This work addresses the problem of predicting the spatiotemporal wind velocity field in the whole flow domain by physics-informed deep learning and LIDAR measurements at sparse spatial locations. The considered LIDAR configuration is illustrated in Fig. 1(A), where two laser beams in the horizontal hub-height 2D plane (shown as the shaded blue area) are used to measure the LoS wind speed in the laser beam directions at a frequency of 1 s at discrete spatial locations along the beams (marked as cross signs in Fig. 1(A)). The half-angle of the beams is 15°. An example of the wind speed measurements by the left and right beams at these discrete locations during a time period from 0 to T is shown in Fig. 1(B). The wind field prediction problem thus states as how to predict the spatiotemporal velocity (including both the downwind and crosswind components) field in the domain of interest (i.e. the whole hub-height 2D flow domain colored in blue in Fig. 1(A)) from time 0 to T based on only the LoS wind speed measurements at a few sparse locations marked as cross signs in Fig. 1(A).

This task is not achievable by using the traditional supervised machine learning framework with whether simple NN such as multilayer perceptions or complex NN such as convolution NN and recurrent NN, because the traditional framework requires the information on the whole spatiotemporal wind field as training data, but in reality only the LoS wind speed data at sparse locations is available. In order to reconstruct the spatiotemporal wind field based on only sparse measurement data, our work employs the novel PINNs framework, where the incompressible NS equations, which provides a very good description for many fluid flows such as atmospheric boundary layer flows, are fused with LIDAR data in the training of the deep learning model.

The overall flowchart illustrating the proposed method is shown in Fig. 1, where the training dataset collection, the deep NN structure and training, and the model prediction are illustrated in Fig. 1(A–B), Fig. 1(C), and Fig. 1(D–E) respectively. The detailed training and prediction process is described in the rest part of this section.

2.1. Training dataset

The training dataset in this work is the LoS wind speed values at sparse spatial locations measured by LIDAR beams. The data measured by the left and right beams are collected separately as the observation process (i.e. the function that maps the flow states to the measurement values) depends on the beam direction. Denote the spatial coordinate of the ith measurement point in the right beam as $[\tilde{x}^r_i, \tilde{y}^r_i]$, the spatial coordinate of the ith measurement point in the left beam as $[\tilde{x}^l_i, \tilde{y}^l_i]$, and the LIDAR measurement values at these coordinates at $\tilde{t}^{th}$ second as $\tilde{u}_{\tilde{x}^r_i,\tilde{y}^r_i,\tilde{t}}$ and $\tilde{u}_{\tilde{x}^l_i,\tilde{y}^l_i,\tilde{t}}$ respectively. We then collect all the LIDAR measurements by the right beam during a time period of T seconds as the data matrix $\tilde{\mathscr{U}}^r$ of shape $[N^r \times T, 4]$, where N^r represents the total number of discrete points in the right beam and each row of $\tilde{\mathscr{U}}^r$ consists of the spatiotemporal coordinate $[\tilde{x}^r_i, \tilde{y}^r_i, \tilde{t}]$ and the corresponding measurement value $\tilde{u}_{\tilde{x}^r_i,\tilde{y}^r_i,\tilde{t}}$. The measurements by the left beam are collected in the same way as $\tilde{\mathscr{U}}^l$ of shape $[N^l \times T, 4]$ with N^l representing the total

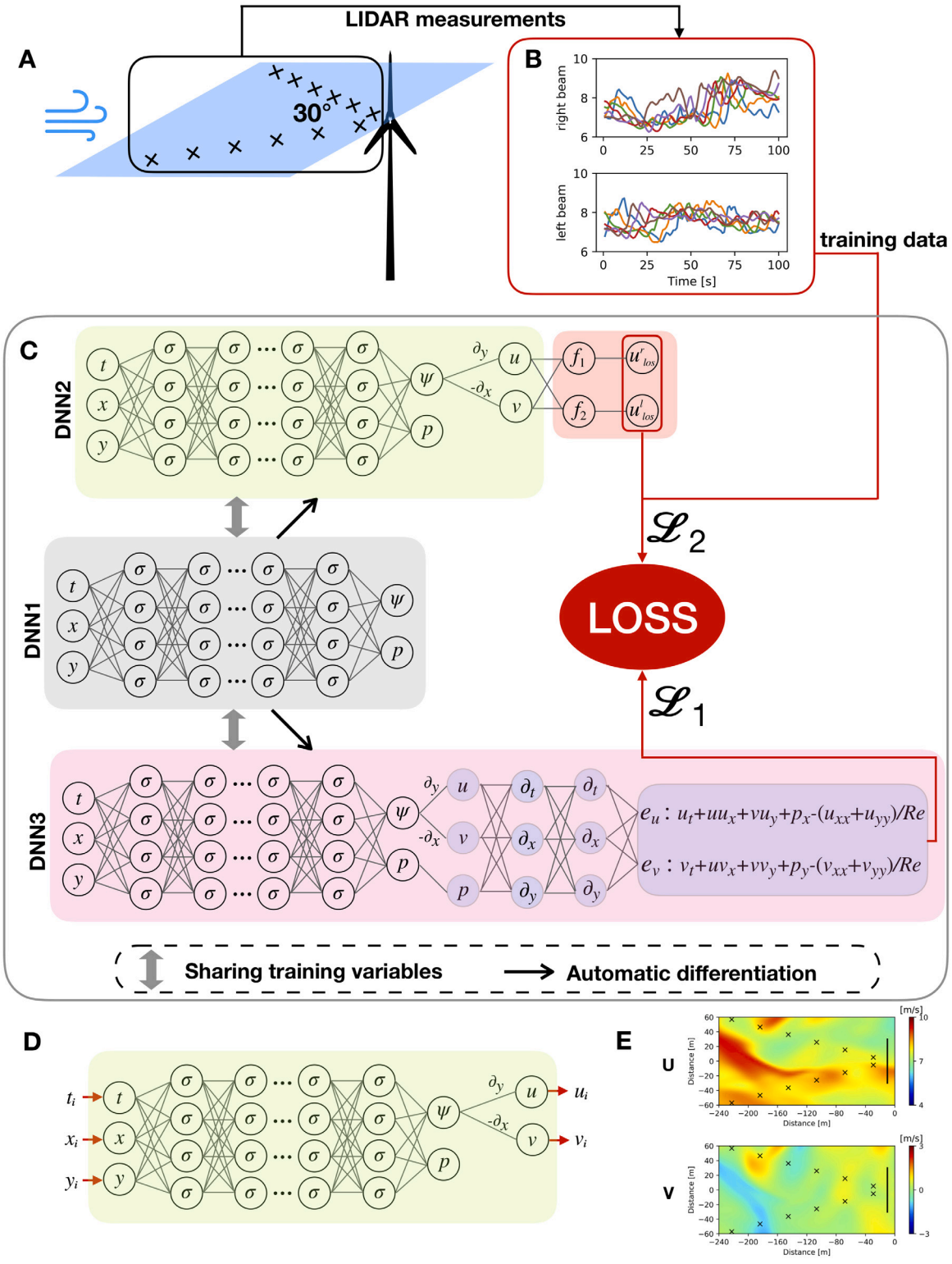

Fig. 1. The flowchart illustrating the proposed spatiotemporal wind field prediction method. (A) LIDAR configuration. (B) The LoS wind speed measured by the left and right laser beams during a certain period. (C) The deep learning model which incorporates the NS equations and LIDAR measurements. (D) The prediction of wind velocity at a given time instant and a given location after NN training. (E) The wind field prediction in the whole domain at a given time instant.

number of discrete points in the left beam. These data matrices are then nondimensionalized by the characteristic length D, the characteristic time D/U_∞, and the characteristic velocity U_∞, where D represents the turbine rotor diameter and U_∞ represents the average freestream wind speed. The nondimensionalized data matrices, which are the only wind data required for the NN training, are hereby denoted as $\mathscr{U}^r$ and $\mathscr{U}^l$. In order to evaluate the trained machine learning model, the test dataset is specified as the spatiotemporal flow field in the whole domain in front of the wind turbine during the same time period T. To avoid confusion, we mention that the training and test dataset in this work are totally different, with the former consisting of the LoS wind speed data at sparse locations and the latter consisting of the wind velocity

vectors at every locations in the 2D plane in front of the wind turbine, while in the supervised machine learning they are generally of the same data structure and are usually obtained by dividing the same dataset.

2.2. Neural network structure

After collecting the training dataset, a fully-connected deep NN is constructed, which is illustrated in shaded gray and denoted as DNN1 in Fig. 1(C). This deep NN takes the nondimensional spatiotemporal coordinate (i.e. $[t, x, y]$) as the input and returns the nondimensional stream function [45] and the pressure as the output (i.e. $[\psi, p]$). It is used to approximate the mapping between the continuous spatiotemporal coordinate and the corresponding quantities, such that given any time instant t_i and any location $[x_i, y_i]$ the deep NN is trained to return $\psi(t_i, x_i, y_i)$ and $p(t_i, x_i, y_i)$ as the output. However, no data about p and ψ is needed for training this NN because these quantities are just auxiliary quantities used for deriving the velocity and encoding NS equations. This fully-connected NN can be expressed in recursive form as

$$\begin{aligned} &H_0 = [t, x, y], \\ &H_i = \sigma(H_{i-1} \cdot W_i + B_i), 1 \le i \le L, \\ &H_L = [\psi, p], \end{aligned} \tag{1}$$

where $L + 1$ represents the total number of layers in this deep NN, $\{W_i, 1 \le i \le L\}$ and $\{B_i, 1 \le i \le L\}$ represent all the training variables in this NN, and σ represents the activation function. The shapes of the weight matrix W_1, $\{W_i, 1 < i < L\}$ and W_L are $[3, N_h]$, $[N_h, N_h]$ and $[N_h, 2]$ respectively, where N_h represents the neuron number of the hidden layers. The shapes of the bias term $\{B_i, 1 \le i < L\}$ and B_L are $[1, N_h]$ and $[1, 2]$ respectively. The total degree of freedom (DoF) of this deep NN (i.e. the total number of training variables) can then be calculated as

$$N_{dof} = 3N_h + (L-2)N_hN_h + 2N_h + (L-1)N_h + 2. \tag{2}$$

The hyperbolic tangent function is used for all the hidden layers in this work and the activation is not applied for the output layer. We mention that L is typically very large. Thus the NN is termed "deep" and it is this deep structure that enhances the ability of the NN in capturing very complex nonlinear dynamics. We mention that fully-connected NN with such large DoF is generally not used in traditional supervised machine learning as the issue of overfitting is hard to tackle, while it can be used in this work as overfitting is constrained by the encoded PDEs in the physics-informed deep learning framework.

After constructing this deep NN, a second NN, as shown in shaded green and denoted as DNN2 in Fig. 1(C), is constructed which takes the nondimensional spatiotemporal coordinate (i.e. $[t, x, y]$) as the input and returns the nondimensional downwind velocity u, crosswind velocity v and pressure p as the output. This second NN is derived based on the first NN, by taking the derivative of the NN output of the first NN with respect to the NN input using automatic differentiation. Thus it shares the same training variables with the first NN and no new training variables are created. The output of this second NN is derived by

$$\partial\psi/\partial y = u, -\partial\psi/\partial x = v. \tag{3}$$

Therefore, the continuity equation

$$\frac{\partial u}{\partial x} + \frac{\partial v}{\partial y} = 0, \tag{4}$$

is satisfied automatically. As LIDAR can only measure the LoS wind speed, no data about u or v is available for the NN training. To train the NN with the LIDAR data, an observation process that maps the flow state (i.e. $[u, v, p]$) to LIDAR observations (i.e. $[u^r_{los}, u^l_{los}]$) is embedded to the second NN, which is shaded in light red in Fig. 1(C). The functions f_1 and f_2 in Fig. 1(C) represent the right and left beam observation processes respectively, which are expressed as

$$f_1(u, v) = u\cos(15°) - v\sin(15°) \tag{5}$$

$$f_2(u, v) = u\cos(-15°) - v\sin(-15°) \tag{6}$$

The inclusion of more LIDAR beams and/or other types of flow sensors such as pressure sensors, is straightforward by embedding the corresponding observation processes in this second NN. In this work, only f_1 and f_2 are embeded as only the measurements from the left and right LIDAR beams are used for the NN training.

Next, a third NN, as shown in shaded pink and denoted as DNN3 in Fig. 1(C), is constructed based on the second NN by taking the derivative of the NN output with respect to the NN input using automatic differentiation. This NN, which is the physics-informed part, takes the nondimensional spatiotemporal coordinate (i.e. $[t, x, y]$) as the input and returns the NS residue terms (i.e. $[e_u, e_v]$) as the output. The NS residue terms are defined by reformulating the following nondimensional 2D NS equations

$$\frac{\partial u}{\partial t} + u\frac{\partial u}{\partial x} + v\frac{\partial u}{\partial y} = -\frac{\partial p}{\partial x} + \frac{1}{Re}\left(\frac{\partial^2 u}{\partial x^2} + \frac{\partial^2 u}{\partial y^2}\right) \tag{7}$$

$$\frac{\partial v}{\partial t} + u\frac{\partial v}{\partial x} + v\frac{\partial v}{\partial y} = -\frac{\partial p}{\partial y} + \frac{1}{Re}\left(\frac{\partial^2 v}{\partial x^2} + \frac{\partial^2 v}{\partial y^2}\right), \tag{8}$$

as

$$e_u = \frac{\partial u}{\partial t} + u\frac{\partial u}{\partial x} + v\frac{\partial u}{\partial y} + \frac{\partial p}{\partial x} - \frac{1}{Re}\left(\frac{\partial^2 u}{\partial x^2} + \frac{\partial^2 u}{\partial y^2}\right) \tag{9}$$

$$e_v = \frac{\partial v}{\partial t} + u\frac{\partial v}{\partial x} + v\frac{\partial v}{\partial y} + \frac{\partial p}{\partial y} - \frac{1}{Re}\left(\frac{\partial^2 v}{\partial x^2} + \frac{\partial^2 v}{\partial y^2}\right). \tag{10}$$

Here $Re = (U_\infty D)/\nu$ with ν representing the kinematic viscosity of air.

In summary, there are three deep NNs constructed in the whole NN structure. However, they are essentially just one NN in terms of training, as all of them share exactly the same training variables and only one loss function will be defined to train these training variables. The NN training and prediction details are described in the next subsection.

2.3. NN training and prediction

The deep NN is trained to minimize the loss arising from both the NS residue terms and LIDAR observations. The loss arising from NS residue terms is defined as

$$\mathscr{L}_1 = \frac{1}{N_{ns}}\sum_{i=1}^{N_{ns}} |e_u(x_i^{ns}, y_i^{ns}, t_i^{ns})|^2 + \frac{1}{N_{ns}}\sum_{i=1}^{N_{ns}} |e_v(x_i^{ns}, y_i^{ns}, t_i^{ns})|^2 \tag{11}$$

where $\{[x_i^{ns}, y_i^{ns}, t_i^{ns}], 1 \le i \le N_{ns}\}$ is a batch of test points which is fed to the deep NN to evaluate e_u and e_v. In practice, a set of test points in the spatiotemporal domain of interest are first collected in a data matrix $\tilde{\mathscr{D}}$ of shape $[N_{test}, 3]$, where N_{test} is the total number of test points and each row of $\tilde{\mathscr{D}}$ contains one spatiotemporal coordinate. Then $\{[x_i^{ns}, y_i^{ns}, t_i^{ns}], 1 \le i \le N_{ns}\}$ is generated by randomly sampling from the data matrix $\mathscr{D}$, which is the data matrix $\tilde{\mathscr{D}}$ nondimensionalized by the characteristic scale D and D/U_∞. In this work, a $81 \times 41 \times 101$ uniform grid points in the domain $[-240, 0]$ m $\times$ $[-60, 60]$ m $\times$ $[0, 100]$ s are used to generate $\tilde{\mathscr{D}}$.

The loss arising from LIDAR observations is defined as

$$\begin{aligned} \mathscr{L}_2 = &\frac{1}{N_{d_1}}\sum_{i=1}^{N_{d_1}} |u^r_{los}(x_i^r, y_i^r, t_i^r) - u_i^r|^2 \\ &+ \frac{1}{N_{d_2}}\sum_{i=1}^{N_{d_2}} |u^l_{los}(x_i^l, y_i^l, t_i^l) - u_i^l|^2 \end{aligned} \tag{12}$$

where $\{[x_i^r, y_i^r, t_i^r, u_i^r], 1 \le i \le N_{d_1}\}$ is a batch of right beam measurement data which are randomly-sampled from the matrix $\mathscr{U}^r$, and $\{[x_i^l, y_i^l, t_i^l, u_i^l], 1 \le i \le N_{d_2}\}$ is a batch of left beam measurement data which are randomly-sampled from the matrix $\mathscr{U}^l$.

Finally, the deep NN is trained to minimize the total loss defined as

$$\mathscr{L} = \mathscr{L}_1 + \mathscr{L}_2, \tag{13}$$

Algorithm 1 The NN training and prediction procedure

1: % The NN training
2: Load LIDAR measurement data, i.e. $\mathscr{U}^r$ and $\mathscr{U}^l$.
3: Load the time and space coordinates of NS test points $\mathscr{D}$.
4: Set training iteration number N_{iter}.
5: Set the batch size N_{ns}, N_{d_1}, N_{d_2}.
6: **for** i in $[1, 2, ..., N_{iter}]$ **do**
7: Generate data batches of size N_{d_1}, N_{d_2} and N_{ns} from $\mathscr{U}^r$, $\mathscr{U}^l$ and $\mathscr{D}$ respectively.
8: Train the deep NN by feeding these data batches to minimize the total loss $\mathscr{L}$.
9: **end for**

10: % The NN prediction
11: Set any time coordinate of interest t.
12: Set a mesh of dimension N_{mesh} for the whole 2D domain.
13: **for** i in [1,2,...,N_{mesh}] **do**
14: Set $[x_i, y_i]$ by the location of the ith mesh point.
15: Propagate $[x_i, y_i, t]$ through DNN2 to predict u and v at the ith mesh point.
16: **end for**
17: The wind field in the whole domain at time t is obtained by combining the u and v predictions at all the mesh points.

by feeding the data batches $\{[x_i^{ns}, y_i^{ns}, t_i^{ns}], 1 \le i \le N_{ns}\}$, $\{[x_i^r, y_i^r, t_i^r, u_i^r], 1 \le i \le N_{d_1}\}$ and $\{[x_i^l, y_i^l, t_i^l, u_i^l], 1 \le i \le N_{d_2}\}$ to the NN simultaneously during each training iteration. The Adam optimization algorithm [46] is employed in this work for the NN training.

After training, the spatiotemporal flow field in the whole flow domain, including both the downwind and crosswind velocity components, can be predicted. Specifically, given any time coordinate t_i and space coordinate $[x_i, y_i]$, the corresponding wind speed u_i and v_i can be predicted through the second NN, as shown in Fig. 1(D). The prediction of the flow field in the whole domain at a given time instant, as shown in Fig. 1(E), can be achieved by propagating the given time coordinate and the space coordinates of all the mesh points in the domain of interest through the second NN. The whole training and prediction procedure is summarized as Algorithm 1. In addition, we mention that after training, the short-term flow field forecasting can also be carried out in a straightforward manner by simply specifying the time t in Line 11 of Algorithm 1 as the time coordinate of interest in the future.

3. Numerical results

The wind field prediction method developed above is evaluated in this section, by using the LES wind farm simulator SOWFA as the experimental platform. The simulation setups are described first, then the spatiotemporal flow field prediction is carried out and the results are validated with the corresponding true values (i.e. the SOWFA simulation results).

3.1. Simulation setups

The LES wind farm solver SOWFA is employed here to simulate the turbulent atmospheric boundary layer. For the mesh generation, as suggested by [43], a uniform mesh of size 12 m × 12 m × 12 m is used in the whole simulation domain of size 3000 m × 3000 m × 1000 m, which is illustrated in Fig. 2. The total number of cells is about 5.2×10^6. 400 s simulations are carried out with a time step of 0.02 s. From the last 100s simulations, the left and right LIDAR measurements are collected, and the corresponding wind field data at turbine hub-height is recorded for validation. In particular, the LIDAR measurement process is simulated by extracting the velocity vectors at the corresponding spatial locations, and then projecting them onto the LIDAR beam directions to obtain the LoS wind speed measurements. The turbine rotor dynamics is excluded in this work, similarly as previous studies [12,13]. We mention that the rotor's blockage effects have impacts on the flow field in the vicinity of the wind turbine [47,48], but the impacts become negligible in the freestream flow further upstream which is the main interested region for this work. The simulation in this work is carried out in local high-performance computing (HPC) clusters, which takes around 2 hours' computational time using 256 processors.

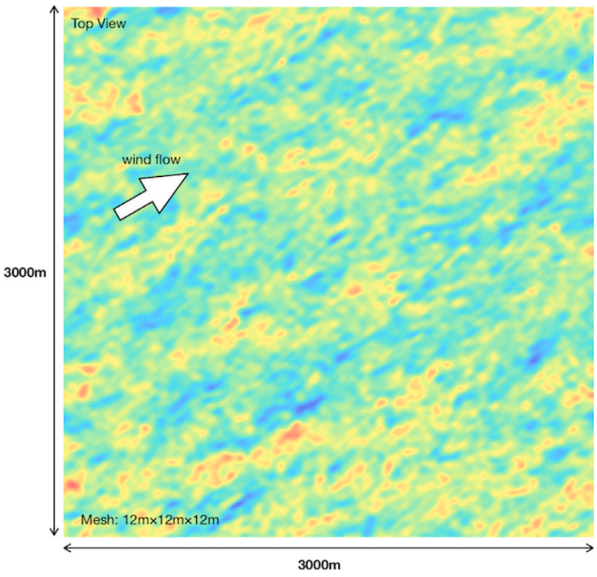

Fig. 2. A top view of the simulation domain at the turbine hub height. The contour shows the instantaneous flow velocity magnitude.

Table 2
The hyper-parameters in the NN structure and the NN training procedure. Here lr represents the learning rate.

L	N_h	N_{ns}	N_{d_1}	N_{d_2}	lr
11	128	1000	1100	1100	10^{-4}

3.2. Performance evaluation

A baseline case is used here to test the performance of the proposed method. For the turbulent atmospheric boundary layer simulations, an average freestream wind speed of 8 m/s with an FSTI level of 6% is considered. For the LIDAR configurations, the range of the LIDAR beams is 220 m and the distance between discrete measurement points is 20 m. There are a total of 11 spatial measurement points per LIDAR beams. The LIDAR measurement is carried out every second during the whole period of 100 s and the measurement noise is excluded. Since the wind turbine usually operates with a yaw angle equal to 0°, the LIDAR look direction is set as the mean wind direction in this baseline case.

There are still some hyper-parameters in the NN structure and the NN training procedure to be determined. The tuning of the hyper-parameters is carried out by trying a set of configurations and comparing their training losses. The hyper-parameters' values used in this work are given in Table 2. As can be seen, the final NN used in this work has a total of 12 layers ($L+1$) and the neuron numbers of the hidden layers are 128. This results in a total DoF of 149 378. This deep structure with such a large DoF enables the NN to accurately approximate complex nonlinear PDE systems such as the NS systems in this work. The further increase of the layer number and the neuron number is tested, which has little impact on the NN's performance. Thus the parameters given in Table 2 are used. The NN training is carried out using the NVIDIA

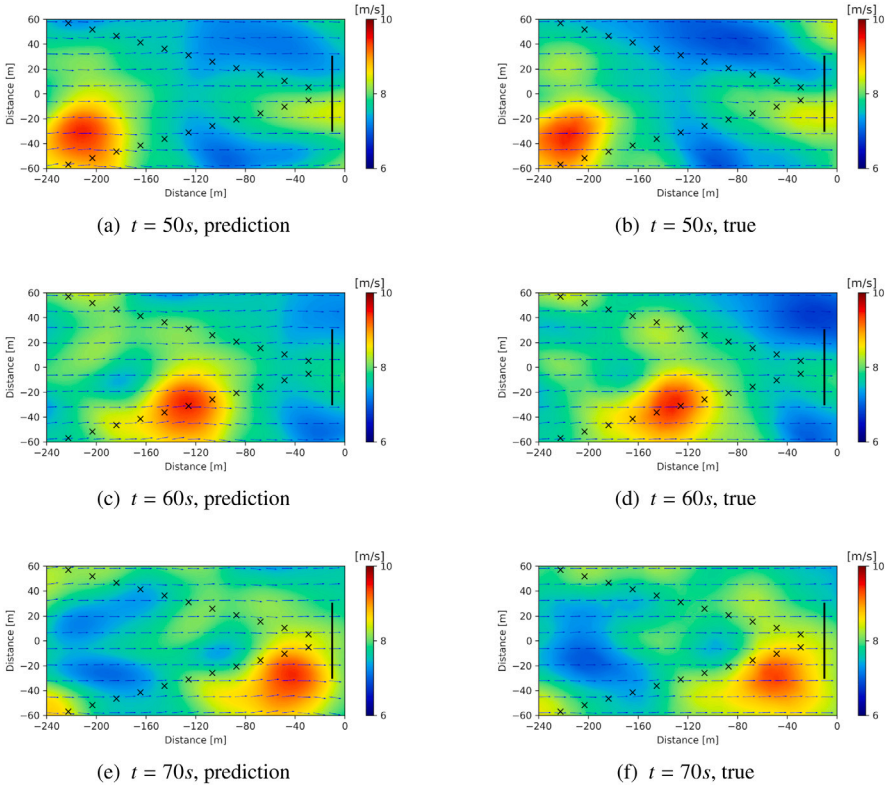

Fig. 3. The velocity field predicted by the proposed method at the baseline case, at time (a) $t = 50$ s, (c) $t = 60$ s and (e) $t = 70$ s. The corresponding true values are also shown for comparisons (b, d, f).

Table 3
The MRMSE between the predicted and the true flow fields during the whole time period, for all the scenarios considered in this work, including (A) the baseline case, (B1-B4) LIDAR measurements with various levels of noise, (C) half spatial resolution, (D) half temporal resolution, (E) 20° LIDAR look direction, and (F) FSTI level of 1%.

Case	Quantity (units)	Range	MRMSE
(A)	Magnitude (m/s)	[6.71, 9.52]	0.198
	Direction (°)	[−6.03, 8.28]	2.77
(B1)	Magnitude (m/s)	[6.71, 9.52]	0.208
	Direction (°)	[−6.03, 8.28]	2.75
(B2)	Magnitude (m/s)	[6.71, 9.52]	0.236
	Direction (°)	[−6.03, 8.28]	3.32
(B3)	Magnitude (m/s)	[6.71, 9.52]	0.387
	Direction (°)	[−6.03, 8.28]	3.73
(B4)	Magnitude (m/s)	[6.71, 9.52]	0.523
	Direction (°)	[−6.03, 8.28]	4.35
(C)	Magnitude (m/s)	[6.71, 9.52]	0.212
	Direction (°)	[−6.03, 8.28]	2.85
(D)	Magnitude (m/s)	[6.71, 9.52]	0.222
	Direction (°)	[−6.03, 8.28]	2.66
(E)	Magnitude (m/s)	[6.70, 9.73]	0.281
	Direction (°)	[11.4, 27.8]	2.46
(F)	Magnitude (m/s)	[6.71, 8.96]	0.204
	Direction (°)	[−6.37, 6.13]	2.69

Tesla K80 GPU in this work with each training iteration requiring about 0.17 s. After training, the prediction of the flow field at any time instant of interest requires about 0.012 s. These demonstrate that the proposed method can meet real-time control requirement by pre-training and online updating. We mention that training schemes based on transfer learning could possibly decrease the computation time, which needs further investigations and is outside the scope of the current work.

After the NN training, the unsteady velocity field during the considered period of 100 s is predicted by the deep NN. Three predicted snapshots, at time $t = 50$ s, $t = 60$ s and $t = 70$ s, along with the corresponding true snapshots (i.e. the snapshots obtained by SOWFA), are shown in Fig. 3. As can be seen, all the predicted snapshots agree with the true snapshots very well. The wind direction and magnitude have been well resolved (Cyclops' dilemma), which is achieved because the correlations between the LoS wind speed measured at different locations are taken into account implicitly through NS residue terms in the NN training procedure. Also, the downstream convection of flow structures in the incoming wind is clearly captured. As shown from the predicted flow fields in Fig. 3(a, c, e), a high-speed flow structure enters the considered flow domain from the left at $t = 50$ s, travels to the middle at $t = 60$ s, and hits the wind turbine at the right side of the domain at $t = 70$ s. This successful identification of the flow structure and its downstream convection are of great interest. For example it can be used for wind turbine control to mitigate the structural loads. In [11], it was shown that significant wind turbine blade load reduction was achievable by taking the coherent flow structures into account in the wind turbine control design. The paper [11] assumed that the coherent structures were known and fully measurable, and pointed out that the prediction of the detailed incoming wind information would play an important role in the level of load mitigation. Therefore, the prediction results in our work fill this research gap by providing an effective way for detailed flow predictions and flow structure detection.

The unsteady wind field visualization is given in the supporting material of this paper, including both the prediction results and the true results given by SOWFA (see Video 1). As shown in the video, the unsteady flow details such as the convections of high-speed/low-speed flow structures, are predicted accurately, which demonstrates the great performance of the proposed prediction method.

To further quantify the accuracy of the proposed method, the mean value of the root-mean-squared errors (MRMSE) between the predicted

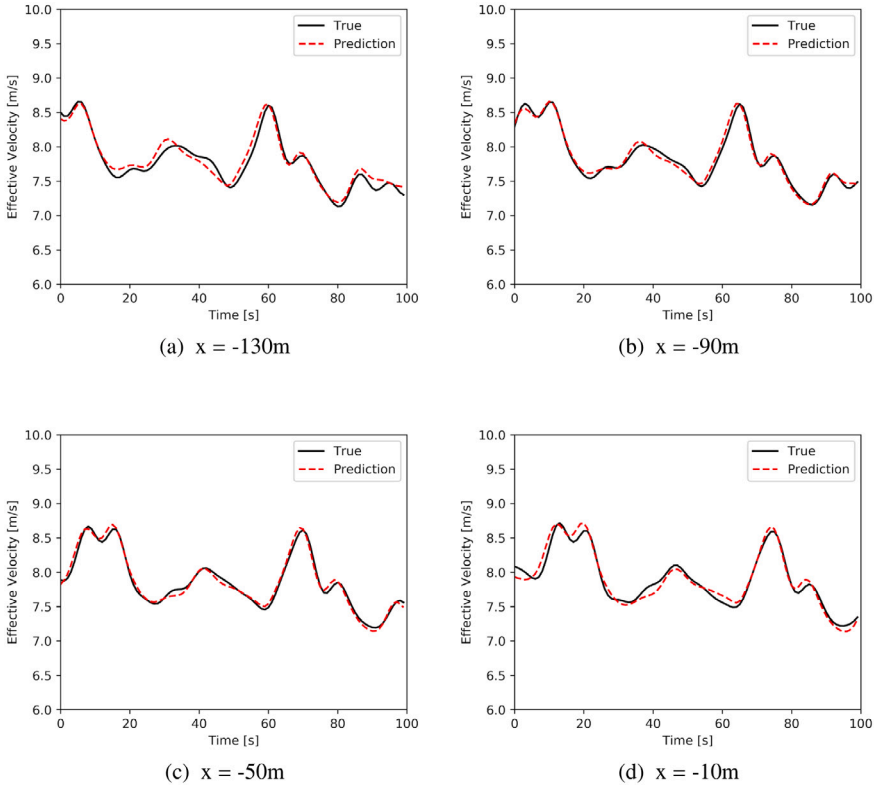

Fig. 4. The effective wind speed predicted by the proposed method for the baseline case at distances of 120 m, 80 m, 40 m, and 0 m before the turbine location. The corresponding true values are also shown for comparisons.

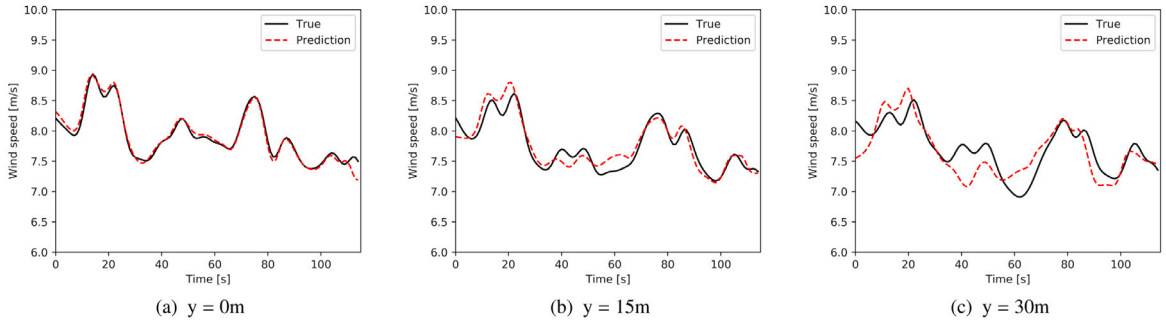

Fig. 5. The instantaneous wind speed at turbine location predicted by the proposed method at the baseline case, at spanwise locations of 0 m, 15 m, and 30 m respectively. The corresponding true values are also shown for comparisons.

and the true wind speed fields during the whole time period is given in Table 3, which is defined as

$$\epsilon_u = \frac{1}{T}\sum_{t=1}^{T}\sqrt{\frac{1}{N_{test}}\sum_{i=1}^{N_{test}}(u^*_{x_i,y_i,t} - \hat{u}_{x_i,y_i,t})^2}, \tag{14}$$

where the total time T is 100, the total number of test points N_{test} is 3321, $\{[x_i, y_i], 1 \le i \le N_{test}\}$ is the 81 × 41 uniform-grid test points in the considered domain, and $\hat{u}_{x_i,y_i,t}$ and $u^*_{x_i,y_i,t}$ represent the corresponding wind speed predictions and true values. Similarly, the MRMSE between the predicted and true wind direction fields is defined as

$$\epsilon_\gamma = \frac{1}{T}\sum_{t=1}^{T}\sqrt{\frac{1}{N_{test}}\sum_{i=1}^{N_{test}}(\gamma^*_{x_i,y_i,t} - \hat{\gamma}_{x_i,y_i,t})^2}, \tag{15}$$

where $\hat{\gamma}_{x_i,y_i,t}$ and $\gamma^*_{x_i,y_i,t}$ represent the corresponding wind direction predictions and true values. As shown in Table 3, the prediction performance is quite satisfactory. The MRMSE is just 7.0% of the freestream wind speed range at this baseline case.

We now demonstrate the potential use of the proposed prediction method for wind turbine control. First the effective wind speed can be extracted from the predicted spatiotemporal wind field, which is defined as the wind speed averaged over the rotor plane and calculated by

$$\bar{U}_{x,t} = \frac{1}{N_y}\sum_{i=1}^{N_y}\hat{u}_{x,y_i,t}, \tag{16}$$

where $\{[x, y_i], 1 \le i \le N_y\}$ is a set of spatial points at a fixed distance before the turbine location and uniformly distributed from $-D/2$ to $D/2$ in the spanwise direction. Fig. 4 shows the effective wind speed averaged over y direction at $x = -130$ m, $x = -90$ m, $x = -50$ m and $x = -10$ m, which correspond to 120 m, 80 m, 40 m and 0 m before the turbine location respectively. The corresponding true values extracted from SOWFA results are also shown. As can be seen, the predicted effective wind speed matches with its true value very well. We mention that the accurate prediction of the effective wind speed is not unexpected as it is calculated based on the accurately-predicted

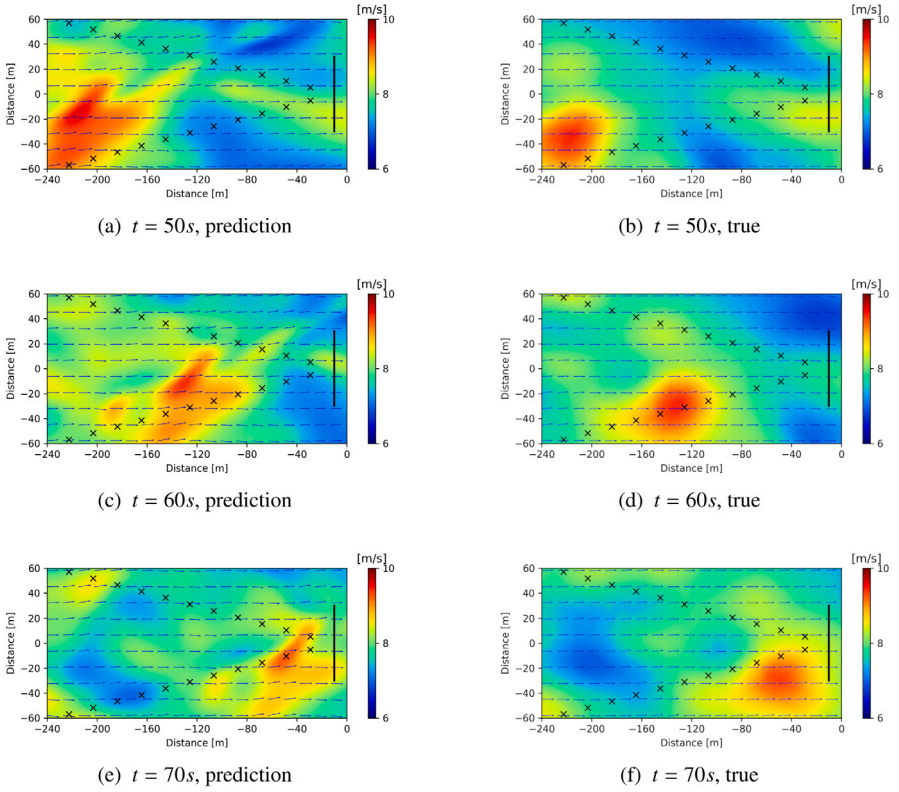

Fig. 6. The velocity field predicted by the proposed method for the case where the measurement noise is of typical commercial LIDAR devices, at time (a) $t = 50$ s, (c) $t = 60$ s and (e) $t = 70$ s. The corresponding true values are also shown for comparisons (b, d, f).

spatiotemporal wind information. This can help wind turbine control e.g. on power regulation and load reduction.

Second, the proposed method can predict the instantaneous wind speed at various turbine locations. As shown in Fig. 5, three spanwise locations, including 0 m, 15 m, and 30 m, are considered, which correspond to the turbine blade root, 1/2 chord length, and turbine blade tip locations. The corresponding true values are also shown in Fig. 5 for comparisons. As can be seen, the predicted instantaneous wind speed matches with its true value quite well. This illustrates the great potential of the proposed prediction method in the control of smart rotors [49].

Last but not least, the proposed method can achieve short-term wind forecasting. The extrapolation of the proposed method to future time instants is examined. In particular, the time coordinates from 100 s to 115 s are fed to the deep NN for predicting the 15-second ahead preview flow information. In order to test the proposed method's performance, another 15 s SOWFA simulations are carried out and the wind field data are recorded. The prediction and the corresponding true results from 100 s to 115 s are included in Fig. 5. As can be seen, the overall instantaneous wind speed is predicted at satisfactory accuracy. This is because the deep NN learns the dynamics of the evolving wind field from NS equations during the training, and the learnt dynamics is retained which enables the deep NN for short-term wind forecasting without using Taylor's frozen turbulence hypothesis [44]. As the machine learning model in this work is continuous in time, any future time coordinate can be fed into the NN for prediction. Thus it avoids the tedious tuning of time steps, time horizons and single-step/multiple-step settings in discrete-time models. However, we mention that as in all other wind prediction models, the prediction time horizon is still limited by the correlations between the data used for predictions and the quantities to be predicted.

3.3. Sensitivity analysis

The robustness of the proposed method is further verified by considering a wide range of scenarios including LIDAR measurements with various levels of noise and under different LIDAR spatial/temporal resolutions, different LIDAR look directions and different FSTI levels. The prediction accuracy under all the considered scenarios is given in Table 3.

Since LIDAR measurements are subject to various error sources such as range weighting, the measurement noise must be considered in real-world applications. Here, the spatiotemporal wind field reconstruction from noisy LIDAR measurements is investigated, where random noise is added to the LoS wind speed value measured by the LIDAR at each measurement location at each time instant. The noise is drawn from the range $[-e, e]$ uniformly and independently, where a set of values of e are considered including 0.025 m/s, 0.05 m/s, 0.1 m/s, and 0.2 m/s. These cases are denoted as Case B1, Case B2, Case B3, and Case B4 in Table 3 respectively. For each case, the deep NN is trained with the noisy measurement data and then used for predicting the spatiotemporal wind field. The prediction MRMSEs for all the four cases are given in Table 3. As expected, the prediction becomes less accurate when the measurement noise increases. However, for all the cases, the errors remain quite small compared to the wind speed range, which demonstrates the method's robustness against noisy measurements. As suggested in [12], Case B3 here represents the typical noise of the commercially available pulsed LIDAR instruments. Similar measurement accuracy has been reported in the product guide of the continuous wave LIDAR devices by ZXLidars (https://www.zxlidars.com). The predicted spatiotemporal flow field for Case B3 is shown in Fig. 6. As can be seen, the unsteady flow field is successfully predicted with main flow structures identified correctly and the MRMSE remains quite small as shown in Table 3, which indicate that the proposed method works well with commercial LIDAR devices. Furthermore, we mention that

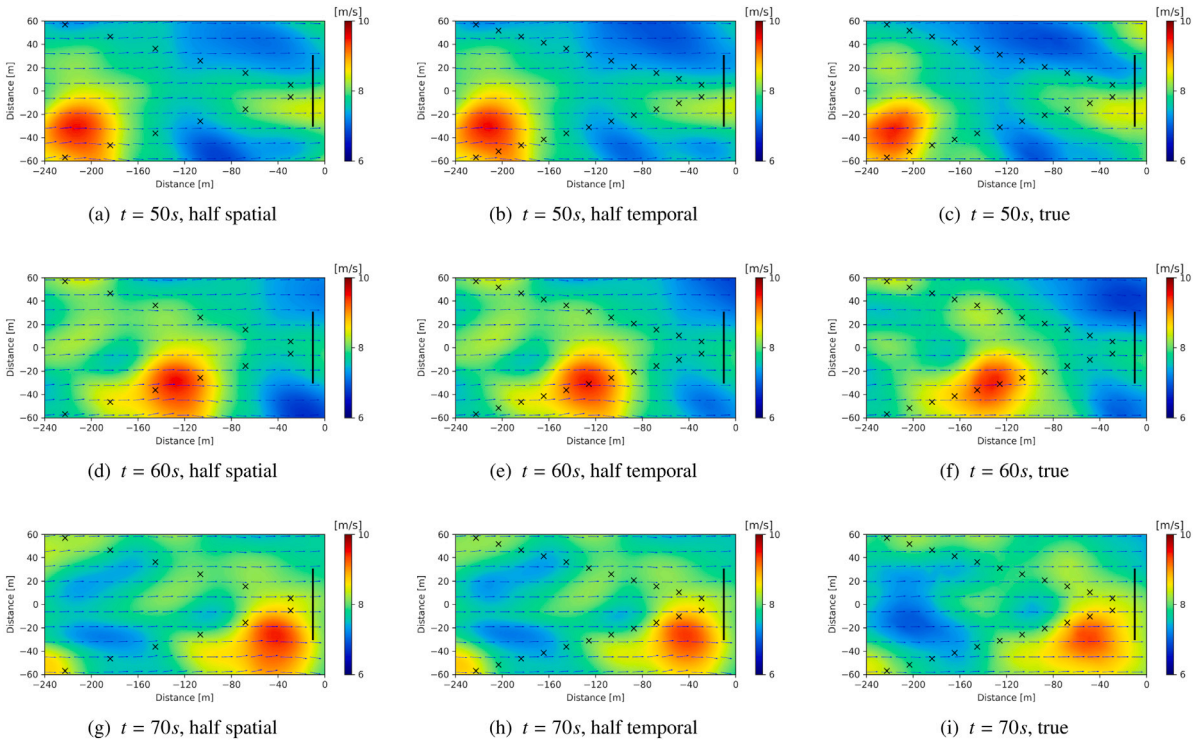

Fig. 7. The velocity field predicted by the proposed method for the cases with low measurement resolutions, at time $t = 50$ s, $t = 60$ s and $t = 70$ s. Sub-figures (a, d, g), (b, e, h) and (c, f, i) are for the cases of half spatial resolution, half temporal resolution and true values respectively.

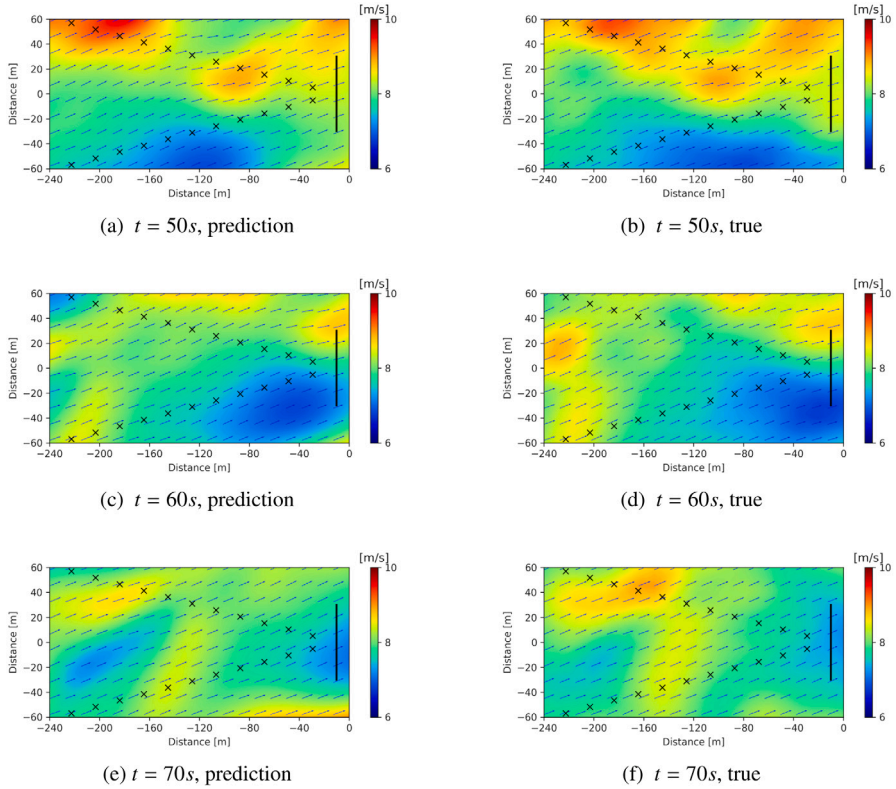

Fig. 8. The velocity field predicted by the proposed method for the case where the LIDAR look direction is 20°, at time (a) $t = 50$ s, (c) $t = 60$ s and (e) $t = 70$ s. The corresponding true values are also shown for comparisons (b, d, f).

new methods such as Bayesian PINNs [32] are under active development, which might offer new opportunities for the predictions with lower-quality measurements.

To further illustrate the proposed method's great performance in predicting the spatiotemporal information from very sparse measurements, the cases with only half spatial/temporal LIDAR measurement

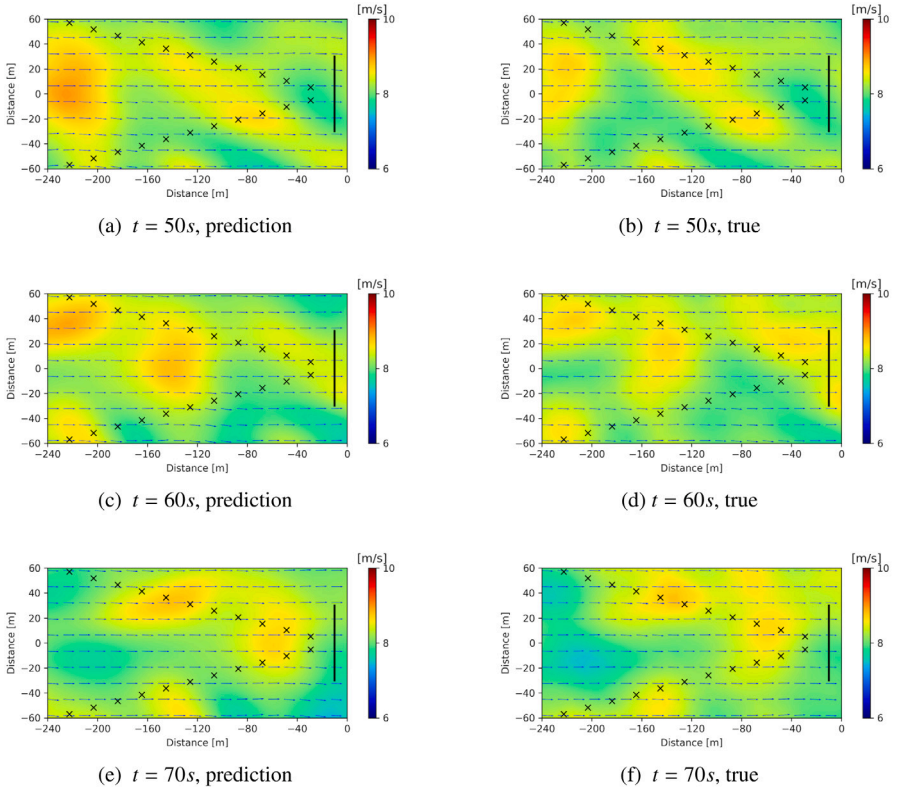

Fig. 9. The velocity field predicted by the proposed method for the case where the FSTI level is 1%, at time (a) $t = 50$ s, (c) $t = 60$ s and (e) $t = 70$ s. The corresponding true values are also shown for comparisons (b, d, f).

resolutions are investigated. For the case with half spatial resolution, the distance between the measurement points is set as 40 m and only 6 measurement points per LIDAR beam are used in the prediction. For the case with half temporal resolution, the measurement frequency of the LIDAR beams is set as 2 s. The prediction results are given in Fig. 7. As can be seen, the flow field predictions are similar as in the baseline case, which demonstrates the method's robustness with various spatiotemporal measurement resolutions. In addition, we mention that the predictions here are based on the measurements at as few as 6 spatial locations per LIDAR beam, while most existing works which follow the PINNs framework have used a much larger set of measurement points. Thus the results here also demonstrate the full potential of PINNs in handling the situations of very sparse data. In addition, the prediction accuracy for the half-spatial case and half-temporal case is just slightly lower than the baseline case, which indicates the existence of data redundancy in the space and time domain for the baseline case. This problem might be solved by designing novel data acquisition strategies for the PINNs to optimally place the measurement locations, which can further increase the data quality and/or reduce the data redundancy. Such strategies might lead to the design of the optimal LIDAR configurations in wind industry, such as optimal half-angles, resolutions, scanning patterns, and even the optimal coordination among LIDAR beams. This task, however, is not trivial and requires extensive studies on the problem formulation and the method development, thus is out of the scope of the current paper.

In addition, as LIDAR can only measure the LoS wind speed, the wind direction needs to be estimated (Cyclops' dilemma). A different LIDAR look direction is also considered here to further demonstrate the proposed method's ability in identifying the incoming wind direction. The incoming wind's mean direction is set as 20° from the turbine facing direction. The results are given in Fig. 8. As can be seen, the incoming wind direction is correctly identified, overcoming the difficulties of estimating wind direction from only LoS wind speed data. The prediction MRMSE given in Table 3 shows that the prediction errors for both wind magnitude and direction remain very small.

Furthermore a different turbulence level is considered, where the FSTI of the turbulent atmospheric boundary layer is set as 1%. The prediction results are given in Fig. 9, along with the corresponding true values. As can be seen, the predictions match well with the true flow fields. The MRMSE given in Table 3 also shows that the proposed method performs very well in this case, similarly as all the other considered cases.

4. Conclusions

In this paper, the prediction of the spatiotemporal wind field based on sparse LIDAR wind speed measurements was investigated by using physics-incorporated deep learning techniques. In order to achieve this, a deep fully-connected neural network (which has a total of 12 layers with the hidden-layer neuron number of 128) was first constructed, and then the Navier–Stokes equations (which provide a very good description of atmospheric boundary layer flows) were incorporated in the neural network structure. The deep neural network structure with a total degree of freedom of 149 378 can approximate complex nonlinear systems governed by partial differential equations (such as the Navier–Stokes system in this work), while the incorporation of Navier–Stokes equations in the neural network training empowers the deep neural network with the ability to learn the dynamics of the evolving flow field over the whole domain of interest, even though the LIDAR measurements are only available at a few sparse spatial locations. To our knowledge, this is for the first time that physical laws and data are fused in a unified manner in the training of deep learning models for wind applications.

The proposed method was evaluated based on the high-fidelity wind farm simulator SOWFA. The results showed that both the wind magnitude and direction were predicted accurately, overcoming the

Cyclops' dilemma. This is because the correlations between the line-of-sight wind speed measured at different locations were taken into account implicitly through the Navier–Stokes residue terms. The unsteady wind field predictions were compared with the corresponding true values. A great match between prediction and true values was observed with the mean value of the root-mean-squared error being only 0.198 m/s for wind magnitude prediction and 2.77° for wind direction predictions at the baseline case. In particular, the flow details such as the propagation of the high-speed/low-speed flow structures were captured by the proposed method. Thus it is expected that the proposed method can lead to a significant reduction of turbine blade structural loads through advanced blade control techniques which take these predicted flow details as control input, especially under the smart rotor concept [49]. To further demonstrate the potential use of the proposed method in wind turbine control, the predictions of the averaged and instantaneous wind speeds were examined. The results showed very good matches between the prediction and true values. In addition, they showed that the proposed method could achieve detailed short-term wind forecasting. These results are apparently also very useful for wind farm control and wind resource assessment. Furthermore, a wide range of scenarios were investigated to demonstrate the proposed method's robustness, which included the LIDAR measurements with various levels of noise and under different LIDAR spatial/temporal resolutions, different LIDAR look directions and different turbulence levels. The results showed that the proposed method performed very well in all these scenarios.

By fusing LIDAR measurements and Navier–Stokes equations, the proposed method achieved great accuracy in spatiotemporal wind predictions. However, we mention that its performance is still limited by the underlying physical law's ability in capturing the full dynamics of the evolving wind. For example, the 3D flow structures and the thermal effects are not captured by the current studies because the employed Navier–Stokes equations are 2D. Therefore, future studies considering more accurate physical models (e.g. 3D Navier–Stokes equations) are needed to improve the prediction performance. In addition, the wind prediction is also limited by the LIDAR measurement data's ability in characterizing the essential wind information. Therefore, it is of great interest to investigate the optimal data acquisition design for the proposed method. It is expected that the data quality will increase using an optimized data acquisition design, which, in turn, will increase the prediction accuracy further. Future research may also include the real-world LIDAR measurement campaign to further validate the proposed method.

As the predicted spatiotemporal flow field contains much more information about the incoming wind than the original LIDAR measurements, it is greatly useful in developing advanced strategies for the wind resource assessment and for the monitoring and control of wind turbine/farm, by using such rich flow information. This may include the usage of the predicted spatiotemporal data for wind power prediction, turbine load evaluation, extreme event forecasting, maintenance scheduling, etc. As the developed method is generic, another research direction is the application of the developed method in the state estimation and forecasting of other systems governed by partial differential equations such as wave/tide energy systems and other flow configurations such as wind over complex terrains.

CRediT authorship contribution statement

Jincheng Zhang: Conceptualization, Data curation, Formal analysis, Investigation, Methodology, Project administration, Software, Validation, Visualization, Writing - original draft. **Xiaowei Zhao:** Conceptualization, Funding acquisition, Investigation, Methodology, Project administration, Resources, Supervision, Writing - review & editing.

Declaration of competing interest

The authors declare that they have no known competing financial interests or personal relationships that could have appeared to influence the work reported in this paper.

Acknowledgments

This work has received funding from the European Union's Horizon 2020 research and innovation programme under the Marie Sklodowska-Curie grant agreement No 765579. The authors also acknowledge the Scientific Computing Research Technology Platform (SCRTP) at the University of Warwick for providing High-Performance Computing resources.

Appendix A. Supplementary data

Supplementary material related to this article can be found online at https://doi.org/10.1016/j.apenergy.2021.116641.

References

[1] Harris M, Hand M, Wright A. Lidar for turbine control. Report No. NREL/TP-500-39154, Golden, CO: National Renewable Energy Laboratory; 2006.
[2] Simley E, Pao L, Kelley N, Jonkman B, Frehlich R. Lidar wind speed measurements of evolving wind fields. In: 50th AIAA aerospace sciences meeting including the new horizons forum and aerospace exposition. 2012, p. 656.
[3] Schlipf D, Cheng PW, Mann J. Model of the correlation between lidar systems and wind turbines for lidar-assisted control. J Atmos Ocean Technol 2013;30(10):2233–40.
[4] Scholbrock A, Fleming P, Schlipf D, Wright A, Johnson K, Wang N. Lidar-enhanced wind turbine control: Past, present, and future. In: 2016 American control conference (ACC). IEEE; 2016, p. 1399–406.
[5] Tong X, Zhao X. Power generation control of a monopile hydrostatic wind turbine using an $\mathcal{H}_\infty$ loop-shaping torque controller and an LPV pitch controller. IEEE Trans Control Syst Technol 2018;26(6):2165–72.
[6] Shu Z, Li Q, He Y, Chan P. Observations of offshore wind characteristics by doppler-lidar for wind energy applications. Appl Energy 2016;169:150–63.
[7] Li J, Wang X, Yu XB. Use of spatio-temporal calibrated wind shear model to improve accuracy of wind resource assessment. Appl Energy 2018;213:469–85.
[8] Dunne F, Simley E, Pao L. Lidar wind speed measurement analysis and feed-forward blade pitch control for load mitigation in wind turbines. Golden, CO: National Renewable Energy Laboratory; 2011.
[9] Yan B, Li Q. Coupled on-site measurement/CFD based approach for high-resolution wind resource assessment over complex terrains. Energy Convers Manage 2016;117:351–66.
[10] Tang X-Y, Zhao S, Fan B, Peinke J, Stoevesandt B. Micro-scale wind resource assessment in complex terrain based on cfd coupled measurement from multiple masts. Appl Energy 2019;238:806–15.
[11] Hand MM, Balas MJ. Blade load mitigation control design for a wind turbine operating in the path of vortices. Wind Energy Int J Prog Appl Wind Power Convers Technol 2007;10(4):339–55.
[12] Towers P, Jones BL. Real-time wind field reconstruction from lidar measurements using a dynamic wind model and state estimation. Wind Energy 2016;19(1):133–50.
[13] Mercieca J, Aram P, Jones BL, Kadirkamanathan V. A spatiotemporal estimation framework for real-world lidar wind speed measurements. IEEE Trans Control Syst Technol 2020;28(4):1595–602.
[14] LeCun Y, Bengio Y, Hinton G. Deep learning. Nature 2015;521(7553):436–44.
[15] Wang H, Li G, Wang G, Peng J, Jiang H, Liu Y. Deep learning based ensemble approach for probabilistic wind power forecasting. Appl Energy 2017;188:56–70.
[16] Liu Y, Qin H, Zhang Z, Pei S, Jiang Z, Feng Z, et al. Probabilistic spatiotemporal wind speed forecasting based on a variational Bayesian deep learning model. Appl Energy 2020;260:114259.
[17] Duan J, Zuo H, Bai Y, Duan J, Chang M, Chen B. Short-term wind speed forecasting using recurrent neural networks with error correction. Energy 2020;119397.
[18] Zhang J, Zhao X. A novel dynamic wind farm wake model based on deep learning. Appl Energy 2020;277:115552.
[19] Ti Z, Deng XW, Yang H. Wake modeling of wind turbines using machine learning. Appl Energy 2020;257:114025.
[20] Ling J, Kurzawski A, Templeton J. Reynolds averaged turbulence modelling using deep neural networks with embedded invariance. J Fluid Mech 2016;807:155–66.
[21] Duraisamy K, Iaccarino G, Xiao H. Turbulence modeling in the age of data. Annu Rev Fluid Mech 2019;51:357–77.

[22] Brunton SL, Proctor JL, Kutz JN. Discovering governing equations from data by sparse identification of nonlinear dynamical systems. Proc Natl Acad Sci 2016;113(15):3932–7.
[23] Rudy SH, Brunton SL, Proctor JL, Kutz JN. Data-driven discovery of partial differential equations. Sci Adv 2017;3(4):e1602614.
[24] Sirignano J, Spiliopoulos K. Dgm: A deep learning algorithm for solving partial differential equations. J Comput Phys 2018;375:1339–64.
[25] Zhu Y, Zabaras N. Bayesian deep convolutional encoder–decoder networks for surrogate modeling and uncertainty quantification. J Comput Phys 2018;366:415–47.
[26] Zhu Y, Zabaras N, Koutsourelakis P-S, Perdikaris P. Physics-constrained deep learning for high-dimensional surrogate modeling and uncertainty quantification without labeled data. J Comput Phys 2019;394:56–81.
[27] Raissi M, Perdikaris P, Karniadakis GE. Physics-informed neural networks: A deep learning framework for solving forward and inverse problems involving nonlinear partial differential equations. J Comput Phys 2019;378:686–707.
[28] Baydin AG, Pearlmutter BA, Radul AA, Siskind JM. Automatic differentiation in machine learning: a survey. J Mach Learn Res 2017;18(1):5595–637.
[29] Yang Y, Perdikaris P. Adversarial uncertainty quantification in physics-informed neural networks. J Comput Phys 2019;394:136–52.
[30] Jagtap AD, Kawaguchi K, Karniadakis GE. Adaptive activation functions accelerate convergence in deep and physics-informed neural networks. J Comput Phys 2020;404:109136.
[31] Meng X, Karniadakis GE. A composite neural network that learns from multi-fidelity data: Application to function approximation and inverse pde problems. J Comput Phys 2020;401:109020.
[32] Yang L, Meng X, Karniadakis GE. B-pinns: Bayesian physics-informed neural networks for forward and inverse pde problems with noisy data. 2020, arXiv preprint arXiv:2003.06097.
[33] Raissi M, Wang Z, Triantafyllou MS, Karniadakis GE. Deep learning of vortex-induced vibrations. J Fluid Mech 2019;861:119–37.
[34] Mao Z, Jagtap AD, Karniadakis GE. Physics-informed neural networks for high-speed flows. Comput Methods Appl Mech Engrg 2020;360:112789.
[35] Raissi M, Yazdani A, Karniadakis GE. Hidden fluid mechanics: Learning velocity and pressure fields from flow visualizations. Science 2020;367(6481):1026–30.
[36] Witha B, Steinfeld G, Heinemann D. High-resolution offshore wake simulations with the les model palm. In: Wind energy-impact of turbulence. Springer; 2014, p. 175–81.
[37] Martínez-Tossas LA, Churchfield MJ, Leonardi S. Large eddy simulations of the flow past wind turbines: actuator line and disk modeling. Wind Energy 2015;18(6):1047–60.
[38] Stevens RJ, Martínez-Tossas LA, Meneveau C. Comparison of wind farm large eddy simulations using actuator disk and actuator line models with wind tunnel experiments. Renew Energy 2018;116:470–8.
[39] Yang X, Milliren C, Kistner M, Hogg C, Marr J, Shen L, et al. High-fidelity simulations and field measurements for characterizing wind fields in a utility-scale wind farm. Appl Energy 2021;281:116115.
[40] Howland MF, Dabiri JO. Wind farm modeling with interpretable physics-informed machine learning. Energies 2019;12(14):2716.
[41] Churchfield M, Lee S. Nwtc design codes-sowfa. 2012, URL: http://wind.nrel.gov/designcodes/simulators/SOWFA.
[42] Churchfield MJ, Lee S, Michalakes J, Moriarty PJ. A numerical study of the effects of atmospheric and wake turbulence on wind turbine dynamics. J Turbul 2012;(13):N14.
[43] Fleming P, Gebraad PM, Lee S, van Wingerden J-W, Johnson K, Churchfield M, et al. Simulation comparison of wake mitigation control strategies for a two-turbine case. Wind Energy 2015;18(12):2135–43.
[44] Taylor GI. The spectrum of turbulence. Proc R Soc Lond A 1938;164(919):476–90.
[45] Batchelor GK. An introduction to fluid dynamics. Cambridge University Press; 2000.
[46] Kingma DP, Ba J. Adam: A method for stochastic optimization. 2014, arXiv preprint arXiv:1412.6980.
[47] Medici D, Ivanell S, Dahlberg J-Å, Alfredsson PH. The upstream flow of a wind turbine: blockage effect. Wind Energy 2011;14(5):691–7.
[48] Zhao F, Wang T, Gao X, Sun H, Yang H, Han Z, et al. Experimental study on wake interactions and performance of the turbines with different rotor-diameters in adjacent area of large-scale wind farm. Energy 2020;117416.
[49] Barlas TK, van Kuik GA. Review of state of the art in smart rotor control research for wind turbines. Prog Aerosp Sci 2010;46(1):1–27.